Journal of Physics: Conference Series **674** (2016) 012002 doi:10.1088/1742-6596/674/1/012002

Subcascade formation ratio in neutron-irradiated stainless steels

T Yoshiie[1], Y Satoh[2], S S Huang[1], M Horiki[1], K Sato[1] and Q Xu[1]

[1]Research Reactor Institute, Kyoto University, Kumatori, Osaka, Japan
[2]Institute for Materials Research, Tohoku University, Sendai, Japan

E-mail: yoshiie@rri.kyoto-u.ac.jp

Abstract. High-energy-particle irradiation in metals produces cascade damage. If the particle energy is high enough, a cascade is divided into subcascades. In each subcascade, a vacancy rich area is surrounded by an interstitial area. Vacancy clusters are expected to form directly in the vacancy rich area. In this study, the vacancy cluster formation ratio in subcascades was estimated by positron annihilation lifetime spectroscopy and transmission electron microscopy in commercial stainless steels and their model alloys. The vacancy cluster formation ratio was 1.7×10^{-3} and 9.1×10^{-5} in austenitic stainless steel and ferritic/martensitic stainless steel, respectively.

1. Introduction

The defect evolution in materials under high-energy-particle irradiation is a multiscale phenomenon. Defect evolution originates from nuclear reactions ($\sim 10^{-22}$ s), followed by point defect formation ($\sim 10^{-13}$ s) and clustering ($> 10^{-10}$ s). Point defect clusters and precipitates change the long-term aging properties of materials. The degradation of mechanical properties is a particularly serious problem for the lifetime of nuclear systems. In order to obtain a unified knowledge of the mechanisms of microstructural development during high-energy-particle irradiation, it is important to understand the collision processes that lead to the formation of localized defects.

High-energy-particle irradiation in metals causes cascade damage, where highly concentrated vacancies are surrounded by interstitials. A high-energy cascade produces subcascades, as shown in Figure 1. In each subcascade, there also exists a vacancy rich area surrounded by an interstitial rich area. In the vacancy rich area, the clustering of vacancies occurs. For most FCC metals, stacking fault tetrahedra (SFT) are mainly formed as vacancy clusters near room temperature. Groups of SFT have been observed by transmission electron microscopy (TEM) [1, 2]. It has been shown that these SFT are formed directly from subcascades, from which the cascade size and the number of subcascades have been estimated [1]. However, the cascade structure of austenitic stainless steels with the FCC structure has not been reported. Furthermore, for BCC metals it is difficult to detect subcascades owing to the lack of SFT formation. Instead of SFT, subcascades in BCC metals lead to micro-voids. However, micro-voids less than 1.5 nm cannot be observed by TEM. Therefore, the understanding of subcascades is lacking in these cases and most information is obtained solely from computer simulations, mainly using molecular dynamics (MD) [3].

Austenitic and ferritic stainless steels are both important nuclear materials. The former have been used primarily as nuclear reactor core materials owing to their high corrosion resistance. Ferritic steels are expected to be used as structural materials in future fusion and fast breeder reactors.

The positron is the only probe that can sensitively detect vacancy-type defects in most materials [4, 5]. If there are open spaces in the lattice, such as vacancies where positively charged nuclei are absent, positrons become briefly trapped in these spaces, resulting in longer lifetimes. The increased lifetime depends on the type and size of defects [6-8], and therefore conveys important information regarding vacancy-type defects.

In this study, the subcascade formation ratio in neutron-irradiated austenitic and ferritic/martensitic stainless steels was studied using TEM and positron annihilation lifetime measurements.

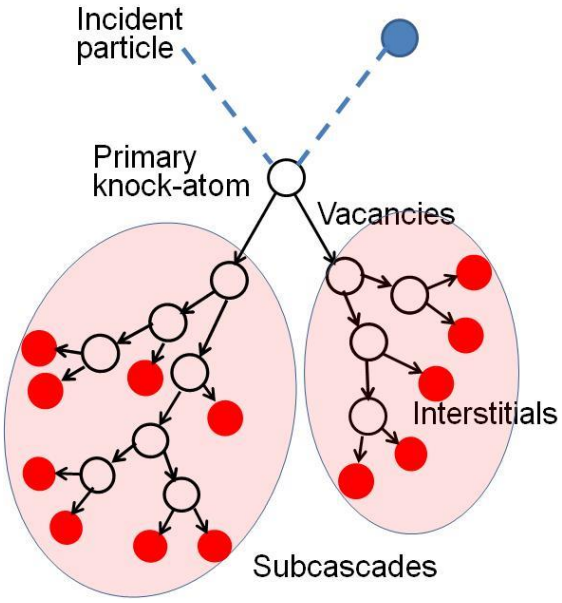

Figure 1. Schematic illustration of subcascades in a cascade.

2. Experimental procedures

The following stainless steel samples were compared in this study: austenitic stainless steel of composition Fe-15.27Cr-15.8Ni-1.88Mn-2.66Mo-0.53Si-0.24Ti-0.055C-0.024P (Ti added modified SUS316SS: JPCA, hereafter referred to as Ti316), model austenitic steel alloys of composition Fe-15Cr-16Ni and Fe-16Cr-17Ni, ferritic/martensitic stainless steel Fe-8%Cr-2%W-0.2%V-0.04%Ta-0.5Mn-0.09Si-0.09C (F82H, referred to as F/MS here) and Fe-8Cr. Each specimen was rolled to 0.1 mm in thickness, from which 3 mm diameter disks were punched out. Ti316, Fe-15Cr-16Ni, and Fe-16Cr-17Ni discs were annealed for 1 h under a vacuum of 1.5×10^{-4} Pa at 1323 K, 1223 K, and 1223 K, respectively. F/MS and Fe-8Cr disks were annealed under high vacuum at 1313 K for 0.5 h and then tempered at 1013 K for 2 hours followed by air cooling. Fission neutron irradiation was performed at the Research Reactor of Kyoto University (6×10^{-4} dpa and 1.5×10^{-3} dpa at 363 K, 1.6×10^{-3} dpa and 5×10^{-3} dpa at 573 K [9]), the Japan Materials Testing Reactor (JMTR) of the Japan Atomic Energy Agency (0.33 dpa at 373 K and 0.11 dpa at 573 K) and Belgian Reactor 2 (BR-2) of the Belgian Nuclear Research Center (0.2 dpa at 363 K and 563 K). Isochronal annealing experiments were performed for 1 h at each temperature after irradiation.

Microstructural observation was performed by a 200 keV TEM, JEOL JEM-2010 at room temperature. Positron annihilation lifetime measurements were carried out at room temperature using a conventional fast-fast spectrometer with a time resolution of 190 ps, corresponding to the full width at half maximum (FWHM). Each spectrum was accumulated at a total of over 1×10^{6} counts for 12 h. The positron lifetime spectra were analyzed using the PALSfit program [10]. To discriminate defect components from bulk components, the lifetime spectrum was decomposed into two or three possible components, a short lifetime τ_1 and two long lifetimes τ_2 and τ_3, based on a trapping model, after

subtracting the radioactive source and background components [10]. To evaluate the size of the vacancy clusters (Vn, where n is the number of vacancies), the experimental results were compared with the calculated positron lifetimes of vacancy clusters. The positron annihilation lifetime of a Fe-14Cr-13Ni model alloy of austenitic stainless steel was calculated based on first principles using Monte Carlo density functional theory in the local density approximation [11]. The calculated lifetimes were 106 ps and 183 ps for positrons annihilated in the matrix and in single vacancies, respectively. These values were almost the same as those of Ni [7, 8], and that is why we used the lifetime of Ni for the identification and estimation of the size of defect clusters such as voids and SFT in Ti316. For the lifetimes of micro-voids in F/MS, those in Fe were used [8]. The lifetimes are summarized in Tables 1 and 2.

Table 1. Positron annihilation lifetimes in Ni [7, 8]. V1 and Vn represent single vacancies and micro-voids of n vacancies, respectively. Two values shown for V5 depended on the orientation of clusters. Sm is a SFT composed of m vacancies.

Size of V clusters	V1	V2	V5	V13	V19	V43	V79	S3	S10	S15	S21	S21	S28
Lifetime (ps)	176	195	264/297	341	371	410	427	183	170	159	155	155	130

Table 2. Positron annihilation lifetimes in Fe [8]. V1 and Vn represent single vacancies and micro-voids of n vacancies, respectively. The two values shown for V2 depended on the orientation of clusters.

Size of V clusters	V1	V2	V5	V9	V15	V27	V51	V59	V65	V137
Lifetime (ps)	180	187/202	246	280	368	396	419	426	427	435

3. Results

3.1. Austenitic stainless steel

The defect structure of Ti316 irradiated at 373 K to a dose of 0.33 dpa is shown in the dark field TEM images of Figure 2, where almost no defects are observed. As a comparison, the defect structure of Fe-Cr-Ni is also shown. In Fe-15Cr-16Ni at 373 K, many SFT and interstitial type dislocation loops are observed. Irradiations at 563 K to a dose of 0.2 dpa and at 573 K to a dose of 11 dpa result in dislocation loops, SFTs, and a few precipitates in Ti316. In Fe-16Cr-17Ni at 563 K to a dose of 0.2 dpa and Fe-15Cr-16Ni at 573 K to a dose of 0.11 dpa, voids are observed in addition to SFT and loops, as shown in Figure 3 of the enlarged photo.

The results of positron annihilation lifetime measurements in Fe-16Cr-17Ni are shown in Figure 4. At 363 K, irradiation to 0.2 dpa results in micro-voids, but the detected intensity was very low, and these voids could not be observed by TEM. At 563 and 573 K, micro-voids are also detected and the intensity is high enough to be observed by TEM. In Ti316, the long lifetimes after irradiation at 363 K and 573 K were somewhat shorter than those for single vacancies. The two or three component analysis was impossible after irradiation to 0.2 dpa at 563 K. These lifetimes correspond to those for vacancies on dislocations, SFT, and interfaces between matrix and precipitates [12]. The annealing behavior of Ti316 irradiated at 363 K to a dose of 0.2 dpa is shown in Figure 6. At 523 K, the lifetime decreased and became similar to that of Ti316 without irradiation. Thus, defects formed at 363 K were not stable. The easy annihilation of defects under 523 K suggests that the lifetime at 363 K is due to single vacancies and vacancies on dislocations.

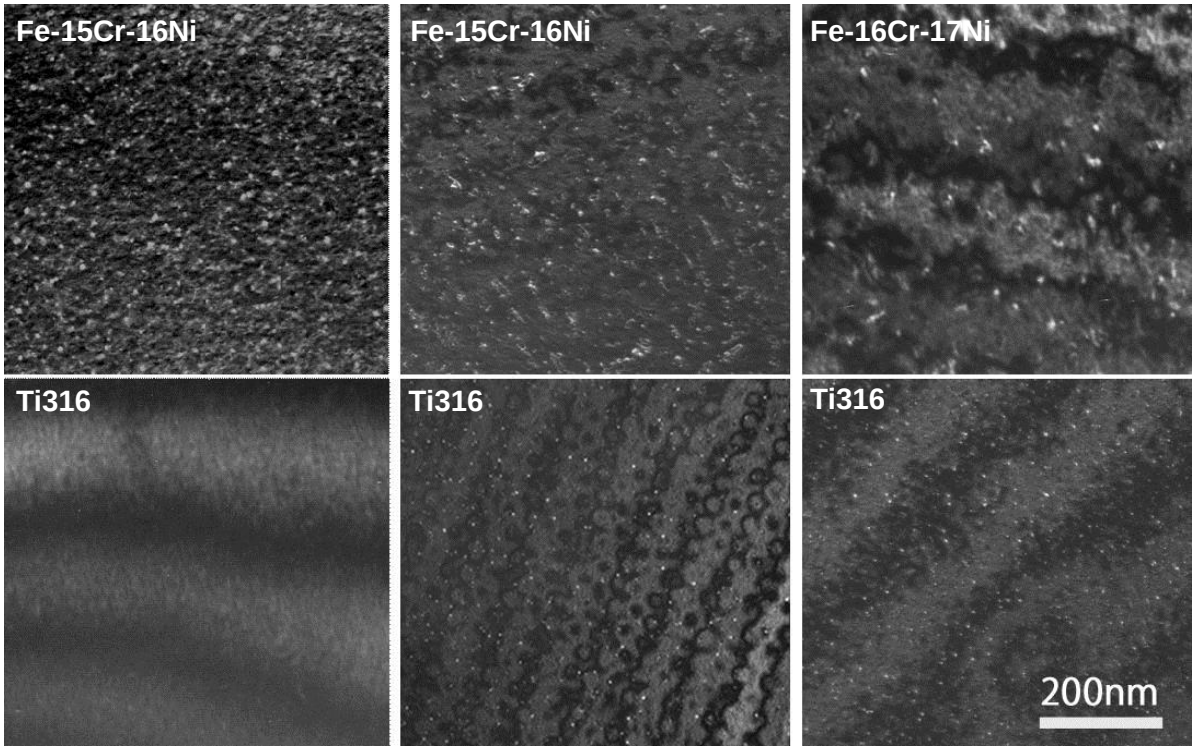

373 K, 0.33 dpa 573 K, 0.11 dpa 563 K, 0.2 dpa

Figure 2. Damaged structures in neutron-irradiated Fe-15Cr-16Ni (373 K and 573 K), Fe-16Cr-17Ni (563 K), and Ti316.

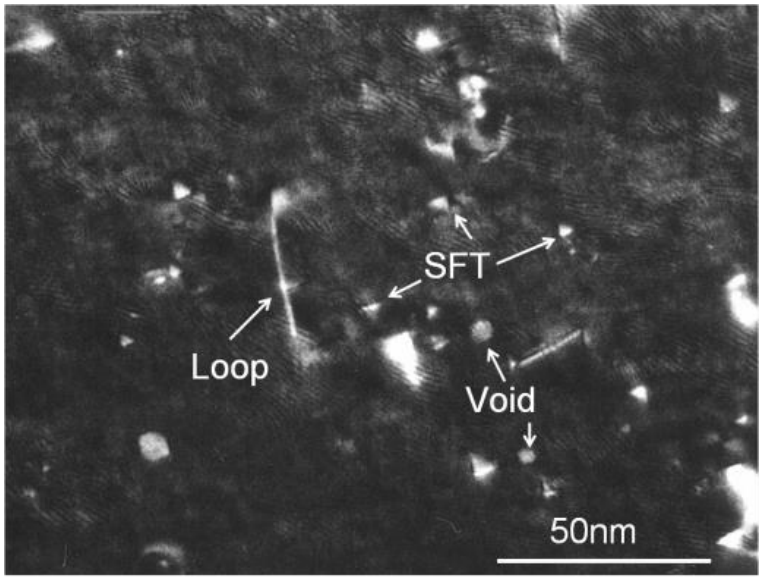

Figure 3. Damaged structures in neutron-irradiated Fe-15Cr-16Ni to a dose of 0.11 dpa at 573 K.

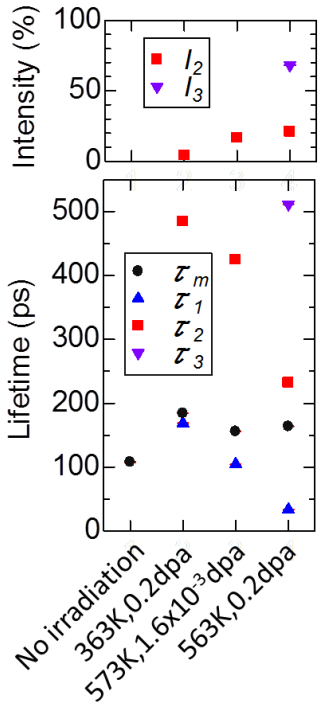

Figure 4. Positron annihilation lifetime measurements of Fe-16Cr-17Ni.

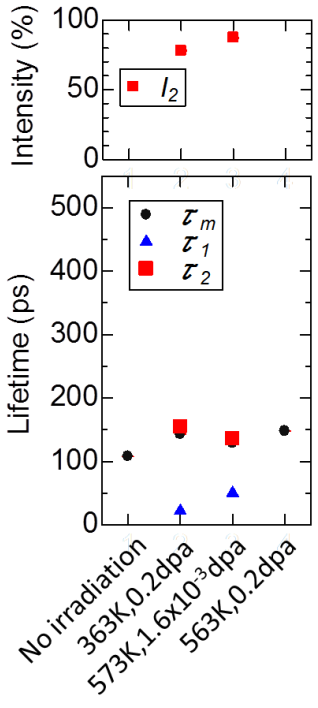

Figure 5. Positron annihilation lifetime measurements of Ti316.

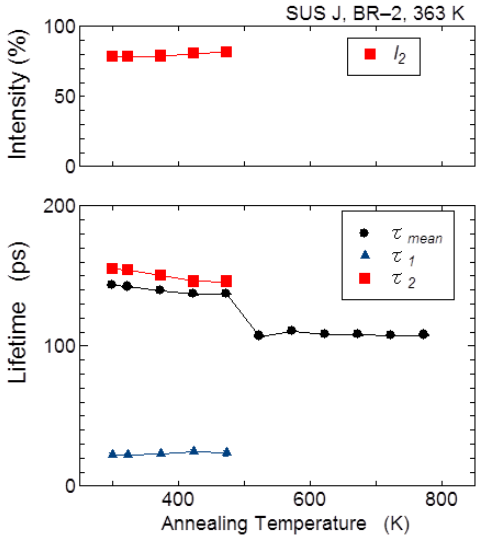

Figure 6. Annealing behavior of neutron-irradiated Ti316 at 363 K to a dose of 0.2 dpa.

3.2. Ferritic stainless steel

Neutron irradiation was conducted for F/MS and Fe-8Cr at 363 K to doses of 6×10^{-4} dpa, 1.5×10^{-3} dpa, and 0.2 dpa, and at 573 K to a dose of 5×10^{-3} dpa. Positron lifetime measurements before irradiation, after neutron irradiation at 363 K and 573 K are shown in Figures 7 and 8. In Fe-8Cr before irradiation, no defects were detected. While in F/MS, a long lifetime of 133 ps was detected. The lifetime can be

attributed to dislocations and interfaces between the matrix and precipitates [12]. After irradiation at 363 K in both Fe-8Cr and F/MS, micro-voids were formed. In F/MS, the average size of micro-voids was 11, 14, and 20 vacancies for doses of 6×10^{-4} dpa, 1.5×10^{-3} dpa, and 0.2 dpa, respectively. After

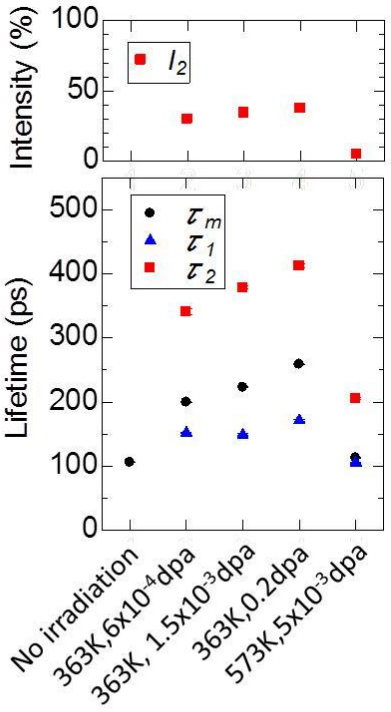

Figure 7. Positron annihilation lifetime measurements of Fe-8Cr.

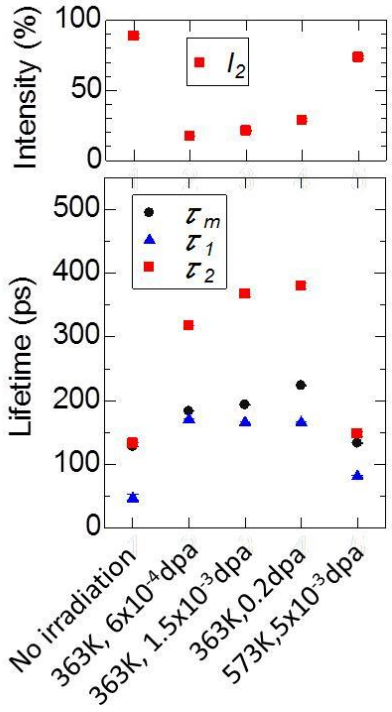

Figure 8. Positron annihilation lifetime measurements of F/MS.

irradiation at 573 K, the mean lifetimes for both alloys were similar to those before irradiation. However, in Fe-8Cr, the lifetime could be decomposed into two components, indicating the formation of defects.

F/MS irradiated at 363 K to 1.5×10^{-3} dpa was isochronally annealed for 1 h at each temperature, as shown in Figure 9. Positron annihilation measurements were conducted after each step at room temperature. A decrease in lifetime was detected after annealing at 573 K. Thus, micro-voids formed at 363 K were not stable at 573 K.

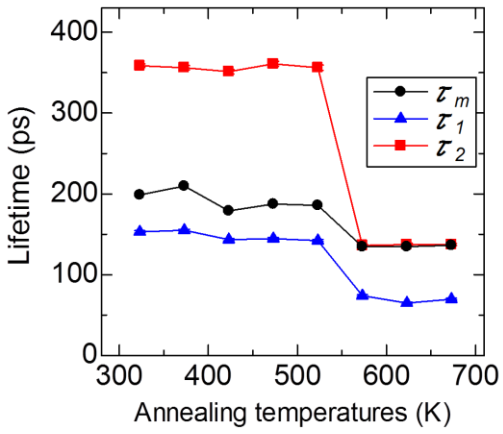

Figure 9. Annealing behavior of neutron-irradiated F/MS at 363 K to 1.5×10^{-3} dpa.

4. Discussion

4.1. Defect structures

The measured τ2 components of positron annihilation lifetime were consistent with TEM observations. In Fe-Cr-Ni irradiated at 363 K and 373 K, vacancies were mobile and accumulated in micro-voids or SFT within vacancy rich areas (subcascades). Vacancies remained in the matrix in TiS16 at 363 K and 373 K, consistent with the fact that vacancies do not move in commercial austenitic stainless steels at 363 K [12]. At 563 K in Fe-16Cr-17Ni and 573 K in Fe-15Cr-16Ni, small SFT annihilated and some SFT and voids grew larger, and could be observed by TEM (Figure 3). In Ti316, only the precipitates grew larger (Figure 5). At this dose range, vacancy-solute diffusion to precipitates prevented vacancy accumulation as micro-voids, as observed in Fe-Cu alloys [13].

In ferritic alloys, no defects were detected in Fe-8Cr prior to irradiation, but in F/MS, precipitates were found. After irradiation at 363 K, micro-voids formed in both Fe-8Cr and F/MS. With increasing dose, the size and concentration of micro-voids increased. For irradiation at 573 K, a few small vacancy clusters, such as V2, remained in Fe-8Cr. These clusters were not stable at 573 K and may form towards the end of the irradiation and remain. For F/MS, void formation was prevented by the growth of precipitates at 573 K, as for Ti316.

The dpa dependence of the trapping rate of the long lifetime at 363 K in F/MS is shown in Table 3, assuming a lifetime of 128 ps (mean lifetime) for F/MS before irradiation. Even before irradiation, defects were present. However, the long lifetime of 133 ps was almost the same as the mean lifetime and we decided that a two state trapping model was appropriate after neutron irradiation at 363 K. The trapping rate is the product of the defect concentration and the capture probability. The capture probability P is calculated from a diffusion model as $P = 4\pi R_T D_+ / \Omega$ [14]. A typical value of 2×10^{-4} m^2/s was used for the diffusion coefficient of positrons, D_+. Ω is the atomic volume. For the trap radius R_T, the radius of micro-voids was used, based on estimates from the long lifetime. With these assumptions, the number density of micro-voids in F/MS at 363 K was 9.8×10^{14}, 1.3×10^{15}, and 1.7×10^{15} $/cm^3$ for capture probabilities of 9.8×10^{-4}, 1.3×10^{-3}, and 2.1×10^{-3}/s, respectively.

Table 3. Trapping rates of neutron-irradiated F/MS at 363 K.

Irradiation dose (dpa)	6.0×10^{-4}	1.5×10^{-3}	2.0×10^{-1}
Capture probabilities (1/s)	9.8×10^{-4}	1.3×10^{-3}	2.1×10^{-3}
Density of micro-voids ($1/cm^3$)	9.8×10^{14}	1.3×10^{15}	1.7×10^{15}

4.2. Subcascade analysis

A primary knock-on atom with a large energy makes several well-separated damaged regions, defined as subcascades. Based on the method for estimating subcascade formation energy proposed by Satoh *et al*. [15], the energy for Ni and Fe was calculated. Simulations of atomic displacement cascades are performed using the binary collision approximation for the systematically varied energy of incident atoms to estimate the break up process of a large cascade into subcascades. The mean distance between collisions that transfer a large amount of kinetic energy to a target atom and the size of the vacancy rich region produced by the target atom are compared as a function of the transferred energy to a target atom. The relation between these two parameters is proposed as a criterion for subcascade formation.

The size of the damaged zone, in which a dense population of vacancies is produced (named here the range of vacancies, R) by cascade collisions of a target atom, is calculated using the MARLOWE code [16]. The relationship between the distance of collisions to produce a target atom (D) and R is proposed to serve as a criterion for subcascade formation, as schematically shown in Figure 10. When D is larger than the range R, two damage zones formed from an incident atom do not overlap each other and become separate subcascades (Figure 10(a)). For example, this condition occurs in Fe at an incident energy above 50 keV (Figure 11). D decreases with the decrease of incident energy, and

begins to cross *R* at an incident energy around 10 keV. Below this energy, *D* is smaller than *R*, and the damaged zones overlap each other (Figure 10(b)). Here the energy divided into a subcascade is determined to be about 10 keV in Fe. By the same procedure, the subcascade formation energy of Ni is also 10 keV. The energy has not yet been obtained experimentally in Fe.

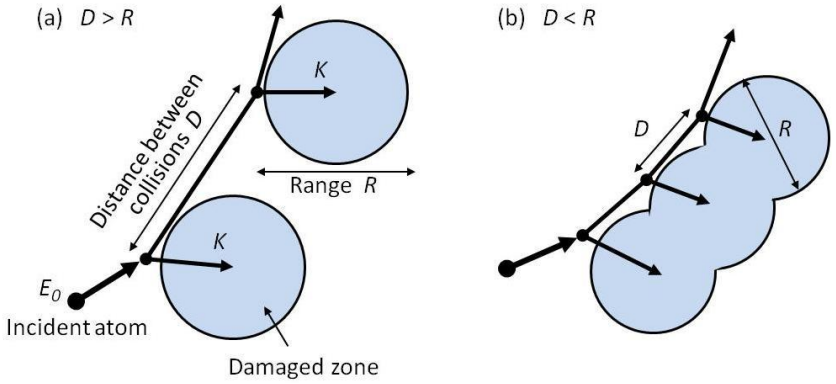

Figure 10. Schematic illustration of the criterion for subcascade formation.

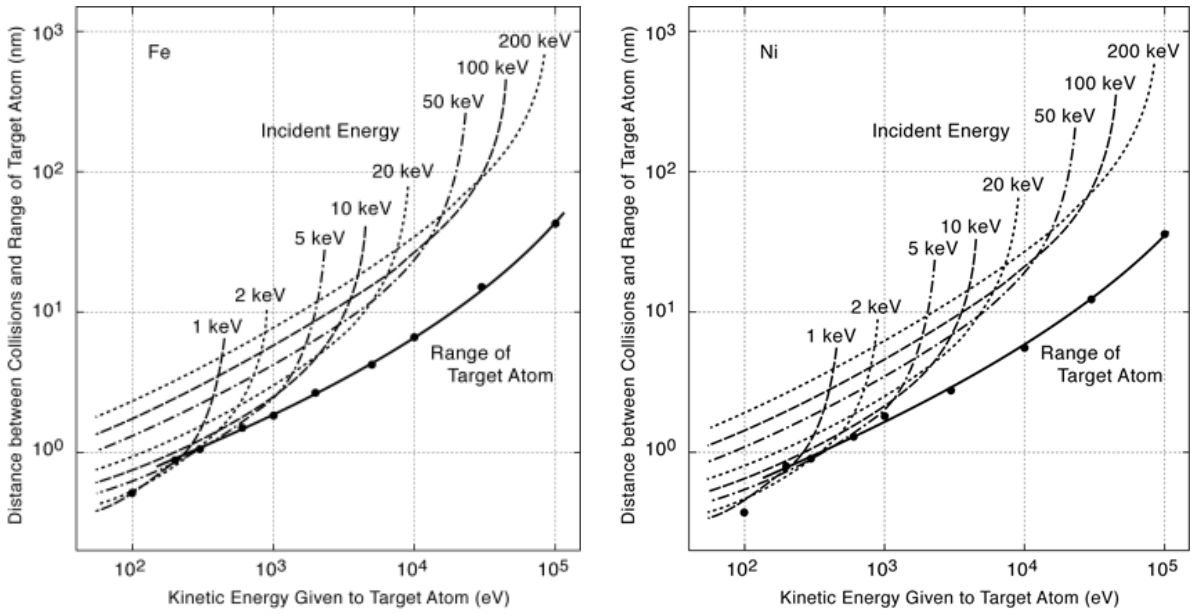

Figure 11. Criterion for the formation of subcascades and subcascade parameters in Fe and Ni. Dotted lines are the mean distance *D* between collisions in which more energy than *K* (horizontal axis) is transferred to the target atom. The bolded line shows the range of vacancies *R* produced by the target atom at its corresponding energy.

The partition of the damage energy *K* to subcascades is determined by assuming a threshold energy for subcascade formation [1] in an analogous procedure as in the Kinchin-Pease model [17] for Frenkel pair production. A damaged area with a deposited energy above the threshold energy E_{SC} is

assumed to evolve into a subcascade. The number of subcascades *Nsc* produced from the primary recoil atom with energy E_{PRA} is

$$\begin{aligned} N_{SC}(E_{PRA}) &= 0 && K(E_{PRA}) < E_{SC} \\ &= 1 && E_{SC} \le K(E_{PRA}) < 2E_{SC} \\ &= \frac{K(E_{PRA})}{2E_{SC}} && 2E_{SC} < K(E_{PRA}), \end{aligned} \quad (1)$$

where $K(E_{PKA})$ is the damage energy for the primary recoil energy E_{PRA}. The cascade formation cross section σ_{CAS} and subcascade formation cross section σ_{SC} are expressed as

$$\sigma_{CAS} = \int_{E_{SC}}^{K_{MAX}} \frac{d\sigma}{dE_{PRA}} dE_{PRA} \quad (2)$$

$$\sigma_{SUB} = \int_{E_{SC}}^{K_{MAX}} N_{SC}(E_{PRA}) \frac{d\sigma}{dE_{PRA}}. \quad (3)$$

The primary recoil energy spectrum $\frac{d\sigma}{dE_{PRA}}$ for the JMTR was calculated using the SPECTER code [18], as shown in Figure 12. In Ni, the total cascade formation cross section was 0.9 barns and the total subcascade formation cross section was 1.6 barns. In Fe, the total cascade and subcascade formation cross sections were 0.86 and 1.3 barns, respectively.

Stoller *et al*. obtained primary damage formation in Fe by MD simulations [3]. In their simulation, 3 large and 3 small damaged areas (subcascades) were formed by 100 keV Fe self-ion irradiation. The number of subcascades in a 100 keV Fe ion in Fe is 5 according to eq (1) with a subcascade formation energy of 10 keV. Their result indicates that a subcascade formation energy of 10 keV in Fe is reasonable.

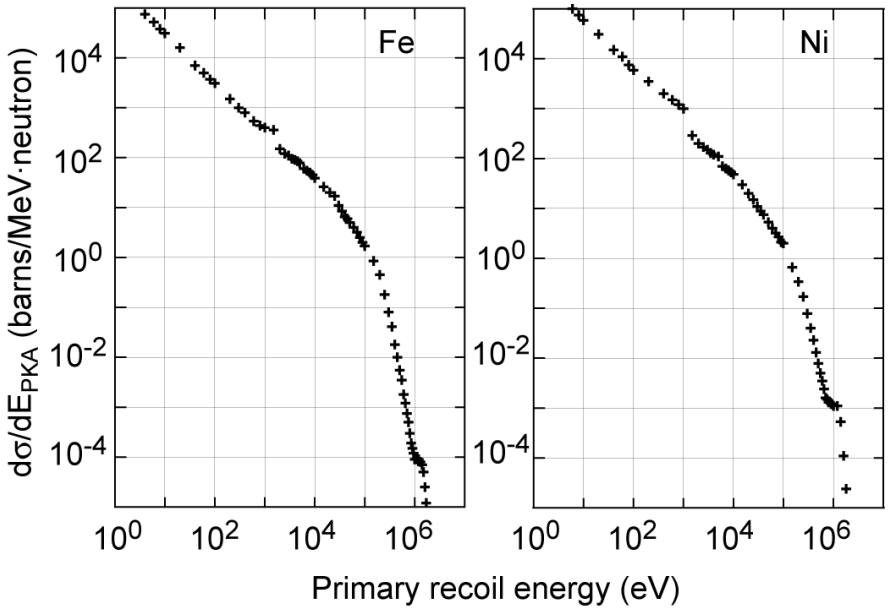

Figure 12. Primary recoil energy spectra of fission neutron-irradiated Fe and Ni as obtained from the SPECTER code [18].

4.3 Sub-cascade formation ratio in stainless steels

In subcascades, vacancy clusters are formed directly, but the production of clusters is not 100%. For Cu, most of the estimated number of subcascades were observed as SFT by TEM [2]. However, for Ni, only a few subcascades were observed as SFT. For austenitic stainless steels, the situation is nearly the same as Ni. Next, we estimate the subcascade formation ratio assuming that SFT were formed in subcascades in Ti316 at 563 K and 573 K, and micro-voids in F/MS at 363 K.

For analyzing the average number density of subcascades (SFT in FCC and micro-voids in BCC), we suppose that there is a volume V around a vacancy cluster in which no additional vacancy clusters can be formed because further cascades eliminate preexisting vacancy clusters through interstitials and simultaneously create new vacancy clusters. In other words, for a number density of preexisting vacancy clusters of ρ, further cascades in a volume ρV per unit volume do not contribute to an increase in the number density of vacancy clusters [19]. The increase of the number density $d\rho$ from an additional fluence $d\varphi$ is expressed as

$$\frac{d\rho}{d\varphi} = N(1 - \rho V)\sigma_{SUB} \tag{4}$$

$$\rho = \frac{1}{V}[1 - \exp(-N\sigma_{SUB}\, V\varphi)], \tag{5}$$

where N is the number density of atoms.

By fitting the dose dependence of SFT in Ti316, V=8.5×10^{-18}cm^3 and σ_{SUB} = 2.7×10^{-3} barns were obtained from eq (5). Figure 13 shows the SFT density and the fit curve using eq (5). The formation ratio of SFT from subcascades was 1.7×10^{-3} by comparing with the subcascade formation cross section of 1.6 barns.

For F/MS, the density of micro-voids obtained in Section 4.1 was used for the analysis. Using the micro-void density ρ in eq (5), V = 5.9×10^{-16} cm^3 and σ = 1.4×10^{-4} barns were obtained. Figure 14 shows the micro-void density and the fit curve using eq (5). The formation ratio of micro-voids from subcascades was 9.1×10^{-5}.

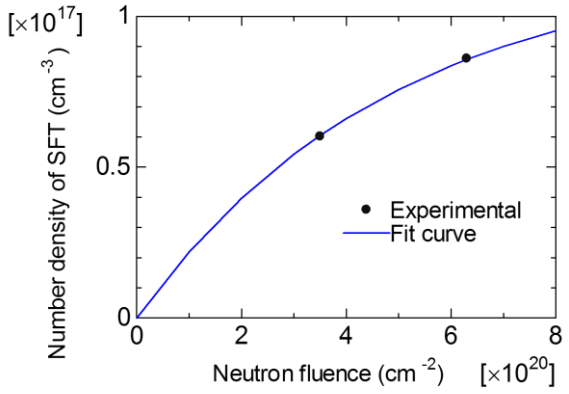

Figure 13. The comparison between experimental results and calculation using eq (5) in Ti316.

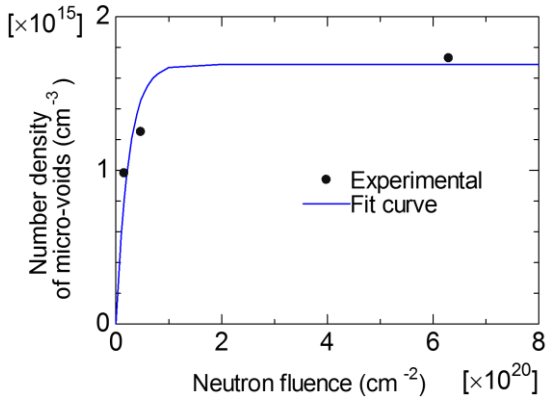

Figure 14. The comparison between experimental results and calculation using eq (5) in F/MS.

Although we obtained values for SFT formation ratio and the micro-void formation ratio, the irradiation facility, irradiation damage rate, and irradiation temperature were different in each irradiation. The damage rate dependence was found to be important for defect evolution [20]. In eq (4), the growth of vacancy clusters directly formed from a subcascade is not taken into account in the present model. The size of the SFT in Ti316 did not change with increasing dose, but in F/MS, micro-

voids grew larger at higher doses. These additional conditions should be considered further in future experiments.

Although there were some ambiguities in the experiments and modelling, the subcascade formation ratio was found to be very low in comparison to that in Au and Cu [1,2]. This observation means that clusters formed directly from subcascades are very unstable. This is probably one of the important reasons for the long incubation period for void swelling in these stainless steels [12, 21-23]. Void swelling begins after high dose irradiation, such as several tenths of a dpa.

5. Concluding remarks

The formation of cascades and subcascades are important for determining the initial state of irradiation damage evolution. No subcascade analyses have been performed in commercial steels prior to this study. In BCC metals, this study determines the subcascade formation ratio for the first time. Although computer simulations have undergone remarkable developments, in particular for the study of cascade structures using MD simulations, comparisons between experiments and simulations are important to ensure the reliability of such calculations. The present study directly addresses this important question.

References

[1] Kiritani M, Yoshiie T, Kojima S and Y. Satoh 1990 *Radiation Effect. Defect. Solid*. **113** 75
[2] Satoh Y, Yoshiie T and Kiritani M 1992 *J. Nucl. Mater*. **191-194** 1101
[3] Stoller R E and Greenwood L R 1999 *J. Nucl. Mater.* **271/272** 57
[4] Brandt W and Dupasquier A 1983 *Positron Solid-State Physics* (North-Holland, Amsterdam)
[5] Dupasquier A and Mills A P Jr 1995 *Positron Spectroscopy of Solids* (Amsterdam: IOS Press)
[6] Shivachev B L, Troev T, Yoshiie T 2002 *J. Nucl. Mater.* **306** 105
[7] Kuramoto E, Tsutsumi T, Ueno K, Ohmura M and Kamimura Y 1999 *Comp. Mater. Sci.* **14** 28
[8] Ohkubo H, Tang Z, Nagai Y, Hasagawa M, Tawara Y and Kiritani M 2003*Mater. Sci. Eng.* A **350** 92
[9] Yoshiie T, Hayashi Y, Yanagita S, Xu Q, Satoh Y, Tsujimoto T, Kozuka T, Kamae K, Mishima K, Shiroya S, Kobayashi K, Utsuro M and Fujita Y 2003 *Nucl. Inst. Meth. Phys. Res* A **498** 522
[10] Kirkegaard P, Olsen J V, Eldrup M and Pedersen N J Riso DTU, February 2009, ISBN 978-87-550-3691-8, 44 p, http://palsfit.dk/
[11] Yoshiie T, Cao X Z, Xu Q, Sato K and Troev T D 2009 *Phys. Status Solidi* **C6** 2333
[12] Yoshiie T, Cao X Z, Sato K, Miyawaki K and Xu Q *J.* 2011 *Nucl. Mater.* **417** 968
[13] Yoshiie T, Xu Q and Sato K 2013 *Nucl. Inst. Meth.* B **303** 37
[14] Puska M J and Nieminen R M 1983 *J. Phys.* F **13** 333
[15] Satoh Y, Kojima S, Yoshiie T and Kiritani M 1991 *J. Nucl. Mater.* **179-181** 901
[16] Robinson M T and Torrens I M 1974 *Phys. Rev.* B **9** 5008
[17] Kinchin G H and Pease R S 1955 *Rep. Prog. Phys.* **18** 1
[18] Greenwood G R and Smither P K 1985 "SPECTER:Neutron Damage Calculations for Materials Irradiation", ANL/FPP/TM-197
[19] Ishida I, Yoshiie T, Sasaki S, Iwase A, Iwata T and Kiritani M 1988 *J. Nucl. Mater.* **155-157** 417
[20] Kiritani M 1989 *J. Nucl. Mater*. **169** 89
[21] Garner F A 1993 *J. Nucl. Mater*. **205** 98
[22] Mansur L K and Coghlan W A 1983 *J. Nucl. Mater.* **119** 1
[23] Tanaka M P, Hamada S, Hishinuma A and Maziasz P J 1988 *J. Nucl. Mater*. **155–157** 801